Journal of Polymer Research (2023) 30:398
https://doi.org/10.1007/s10965-023-03785-5

ORIGINAL PAPER

Coarse-grained molecular dynamics simulation on strain-hardening and fracture behaviors of polycarbonate: Effect of polydispersity and spatial distribution

Tatchaphon Leelaprachakul[1] · Atsushi Kubo[2] · Yoshitaka Umeno[2]

Received: 29 May 2023 / Accepted: 15 September 2023 / Published online: 6 October 2023

Abstract
Coarse-grained molecular dynamics simulation of polycarbonate is utilized to investigate the relationship between molecular structure (i.e., polydispersity and molecular spatial distribution) and strain-hardening and fracture behavior of polycarbonate. We find that strain-hardening modulus and chain extensibility, which are the constitutive parameters of the Eindhoven Glassy Polymer model are highly affected by spatial distribution but are insensitive to polydispersity. This is attributed to the higher rate of nonaffine deformation in the structure with a high radius of gyration. On the other hand, maximum stress at fracture is highly influenced by both spatial distribution and polydispersity due to the ability to sustain entanglements at larger strain. We suggest the phenomenological expression of maximum stress as a function of the radius of gyration, the number of entanglements, and polydispersity.

Keywords Polycarbonate · Coarse-grained molecular dynamics · Molecular structure · Radius of gyration · Strain-hardening modulus · Fracture

Introduction

Polycarbonate (PC) is a versatile amorphous thermoplastic material widely used in various applications ranging from automotive components to electronic devices. This is owing to its well-known properties, such as high-impact resistance, thermal stability, and optical transparency [1]. These excellent mechanical responses of polycarbonate are attributed to its molecular structure [2]. The molecular structure of polycarbonate is a system of macromolecular chains consisting of the arrangement of spatially distributed monomers restricted by topological constraints or molecular entanglements by neighboring chains. This molecular configuration plays a crucial role in determining the material's stress-strain behavior when subjected to uniaxial tension [3]. Understanding the influence of molecular structure on mechanical response is essential to develop the material's performance.

The selection of the constitutive model and parameters used in numerical simulations, the finite element method (FEM), holds a critical role in describing the mechanical or stress-strain behaviors of PC. It is widely acknowledged that the molecular structure of polymers profoundly influences their mechanical properties [2]. Previous research has focused on experimental data fitting rather than insights from molecular dynamics simulations to obtain the constitutive parameters [3–6]. As a result, the intricate relationship between molecular structure and stress-strain behavior, as well as the underlying mechanisms, remains inadequately explained in existing studies.

The deformation behavior of polycarbonate can be categorized into three regions: pre-yield, post-yield, and fracture [4, 7]. The pre-yield behavior is purely elastic and consistent across all polycarbonate samples [7]. In the post-yield region, the constitutive Eindhoven Glassy Polymer (EGP) model is employed to describe deformation behavior in this study [4, 8, 9]. The EGP model characterizes strain-hardening

✉ Yoshitaka Umeno
umeno@iis.u-tokyo.ac.jp

Tatchaphon Leelaprachakul
tachaphon@ulab.iis.u-tokyo.ac.jp

Atsushi Kubo
kubo@ulab.iis.u-tokyo.ac.jp

[1] Department of Mechanical Engineering, The University of Tokyo, Hongo, Bunkyo 113-8654, Tokyo, Japan

[2] Institute of Industrial Science, The University of Tokyo, Komaba, Meguro 153-8505, Tokyo, Japan

behavior through two parameters: the strain-hardening modulus (G_r) and chain extensibility (α) [4]. Within the strain-hardening region, the rate of local plastic activity is directly proportional to the strain-hardening modulus [10, 11], and this local plastic activity can be quantified in MD simulations using nonaffine particle displacement. However, the EGP model has limitations in characterizing the fracture behavior of polycarbonate, as the maximum stress is influenced by various molecular parameters, including molecular weight, polydispersity index (PDI), the radius of gyration (R_g), and molecular entanglement [12, 13]. The examination of the influence exerted by the polydispersity index and the radius of gyration on both the parameters of the EGP model and the maximum stress, therefore, represents a prospective avenue for gaining valuable insights into the enhancement of the mechanical properties of polycarbonate in the future.

While the molecular structure and behavior are difficult to observe and examine in conventional experimentation, a molecular dynamics (MD) simulation provides insight into atomic interaction and position over time during the application or testing. There are two techniques of MD: all-atom molecular dynamics (AAMD) and coarse-grained molecular dynamics (CGMD) simulations. In CGMD simulation, a group of atoms is treated as a single coarse-grained particle [14]. The simplification reduces the computation time, allowing for a more extensive system and/or a more extended simulation. The principal advantage of computational simulation over experimental investigation is that it allows direct quantification of the molecular structure that affects macroscopic response.

The mechanical response of polycarbonate has been the subject of investigation in multiple recent studies, using both AAMD [10, 15–18] and CGMD [7, 12, 13, 19–25] simulations of tensile loading studies to gain insight into the behavior of this material. However, these MD studies investigated only either monodisperse models [7, 12, 19, 20, 22, 25] or a typical realistic distribution of molecular weight model [10, 15, 16]. These MD models were not appropriate for the investigation of the effect of molecular weight distribution on strain-hardening and fracture behaviors and the evolution of molecular entanglement of PC. Nevertheless, experimental studies of polycarbonate have indicated that the degree of molecular weight distribution measured by polydispersity index (PDI), which is defined as the ratio of weight-average molecular weight (M_w) and number-average molecular weight (M_n), i.e., PDI = M_w/M_n, can be a significant factor characterizing the mechanical performance of polycarbonate [8, 26–28]. Additionally, recent studies revealed that the spatial distribution of each polymeric chain, which is quantified by the radius of gyration and segment length, also affects the deformation behaviors of polycarbonate [10, 12, 13, 29]. Therefore, it is urged to investigate how PDI and radius of gyration affect the strain-hardening and fracture behaviors of polycarbonate.

This study employs CGMD to investigate the influence of the polydispersity index and spatial distribution on the molecular behavior of glassy polycarbonate when subjected to uniaxial tensile deformation. Through the construction of a series of coarse-grained models characterized by the polydispersity index and radius of gyration, the research examines the effects of these two molecular parameters (PDI and R_g) on two constitutive EGP model parameters (G_r and α) in post-yielding strain-hardening region and maximum stress at fracture in detail. The strain-hardening modulus and chain extensibility of each structure are determined using the EGP model, and a mathematical expression is proposed to describe the maximum stress as a function of the polydispersity index, the radius of gyration, and molecular entanglement. The findings of this study contribute to the advancement of the understanding of the effect of the molecular structure of polycarbonate on strain-hardening and may inform future efforts to optimize these properties.

Methodology

Coarse-grained particle model

The composition of a polycarbonate unit includes three different atomic arrangements: carbonate, phenylene, and isopropylidene, identified as particles A, B, and C, as shown in Fig. 1. The study employed Kubo et al.'s coarse-grained (CG) model [19], which reduces 33 atoms to four CG particles. This model decreases the simulation's degree of freedom by about 90% compared to the all-atom model, primarily by combining implicit hydrogen with the CG particle. As a consequence, this simulation can be up to 1000 times faster than the all-atom model.

The model defines potential energy into two sources: intermolecular interaction (E_{inter}) and intramolecular interaction (E_{intra}). The intermolecular interaction originates from the non-bonding interaction determined by Morse's potential with a cut-off radius of 12 Å

$$E_{inter} = \sum_{i<j} D_0 \left\{ \exp\left[-2\beta(R_{ij} - R_0)\right] - 2\exp\left[-\beta(R_{ij} - R_0)\right] \right\}, \quad (1)$$

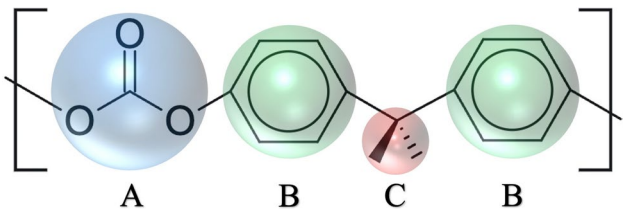

Fig. 1 Schematic of a polycarbonate (PC) molecular structure and coarse-grained CG representation. Particles **A**, **B**, and **C** represent carbonate, phenylene, and isopropylidene, respectively

where R_{ij} is the displacement between a pair of non-bonded particles *i-j*; potential parameters D_0, β, and R_0 are the constants of Morse's potential determined for each combination of particles in an all-atom model.

The intramolecular interaction originates from the bonding interaction and angle interaction and is expressed by

$$E_{\text{intra}} = \sum_{b:\text{bond}} \sum_{l=2}^{4} K_l^{\text{b}} \left(b - b_0\right)^l + \sum_{\theta:\text{angle}} \sum_{m=2}^{4} K_m^{\text{a}} \left(\theta - \theta_0\right)^m, \tag{2}$$

where b and θ are the bond length and bond angle, respectively, within an individual molecular chain; the potential parameters K_l^{b}, K_l^{a}, b_0, and θ_0 are constants determined for all combinations of bond length and bond angle types in an all-atom model. In the context of the physical properties, the parameters b_0 and θ_0 symbolize equilibrium bond lengths and bond angles, respectively. Recent research [19] has investigated the specific values of these parameters, which are presented in Table 1 for reference. All potential parameters are identical to the recent research on polycarbonate [19]. In the CG representation, PC chains are stretched in a linear conformation during the deformation, and the dihedral term cannot be evaluated. Thus, the model does not include the dihedral term. Given that limited bond breaking is observed during polycarbonate fracture, it is notable that the model does not consider bond breaking [16].

Coarse-grained particle arrangement and radius of gyration control

The arrangement of CG particles within polycarbonate follows an equilibrium positioning strategy [13], wherein each particle is positioned in optimal equilibrium with the preceding particle along the chain (molecule). Noting that the first particle of the chain is placed in a random position in three-dimensional space. In the context of this study, the placement of CG particles is constrained by the equilibrium bond lengths (b_0) and bond angles (θ_0) on a two-dimensional plane, with the torsional angle (ϕ) maintained at zero. This constraint is upheld until a specified number of monomers, referred to as the segment length, is attained. Subsequently, a random torsional angle is assigned to the particle. A schematic illustration of the polycarbonate configuration generation process is presented in Fig. 2. Notably, for a chosen segment length of three monomers, the random value selection applies to ϕ instead of zero as depicted in Fig. 2, while θ remains fixed at θ_0 or 76 degrees.

Upon increasing the segment length, a corresponding increase in the radius of gyration is observed. Manipulating the segment length enables precise control over the radius of gyration within the polycarbonate structure. Figure 3 shows an example of a configuration generated with a segment length of 16 monomers. The following section will show the correlation between segment length and the resulting radius of gyration.

Table 1 Equilibrium bond lengths (b_0) and bond angles (θ_0) of CG potential intramolecular parameters for PC [19]

	A-B	B-C	
b_0 (Å)	3.70	3.40	
	A-B-C	B-A-B	B-C-B
θ_0 (degree)	180	180	76.0

Preparation of simulation cells

Polycarbonate simulation cells were prepared with nine different M_{w} ranging from 32.8 to 50.95 kg/mol, with an identical M_{n} = 32.8 kg/mol; therefore, there were nine different polydispersities of polycarbonate systems prepared for the investigation ranging from 1.00 to 1.56. The details and molecular distribution of the simulation cell are shown in Table 2. The study considered three different sizes of molecular chains: 32-monomer, 128-monomer, and 224-monomer, denoted as short, medium, and long chains, respectively. The monodisperse (PDI = 1.00) polycarbonate system is composed of 32 medium chains. To increase M_{w}, four medium chains were split into two short and two long chains equally. The total molecular chains and M_{n} of the system remain the same at 32 chains and 32.8 kg/mol, respectively, but M_{w} gradually increases, and the length of the cubic structure is around 11 nm, see Fig. 4a. The study also addresses an issue related to simulation cell size, which is further elaborated in Appendix A of the research. The artificially polydispersed polycarbonate systems were used to study the effect of the presence of various sizes of molecular chains within the same polymer system on its molecular behavior and mechanical performance.

The spatial distribution of the polymeric chain is quantitatively described by the chain radius of the gyration

$$R_{\text{gc}}^2 = \frac{\sum_{i=1}^{N_{\text{p}}} m_i \left(\Delta \mathbf{r}_i\right)^2}{\sum_{i=1}^{N_{\text{p}}} m_i}, \tag{3}$$

where N_{p}, m_i, and $\Delta \mathbf{r}_i$ are the number of particles, the mass of particles, the relative position of particle i with its center of mass of each molecular chain, respectively. The root-mean-square of the chain radius of gyration determines the spatial distribution of the polymer system and is denoted as R_{g}.

To quantify the spatial distribution of mass-distributed structure, the root-mean-square radius of gyration normalized by molecular weight is used to describe the mechanical performance of the polycarbonate and is expressed as

$$R_{\text{g}}^{\text{n}} = \sqrt[2]{\frac{1}{N_{\text{c}}} \sum_{j=1}^{N_{\text{c}}} \frac{R_{\text{gc}}^2}{M_j}}, \tag{4}$$

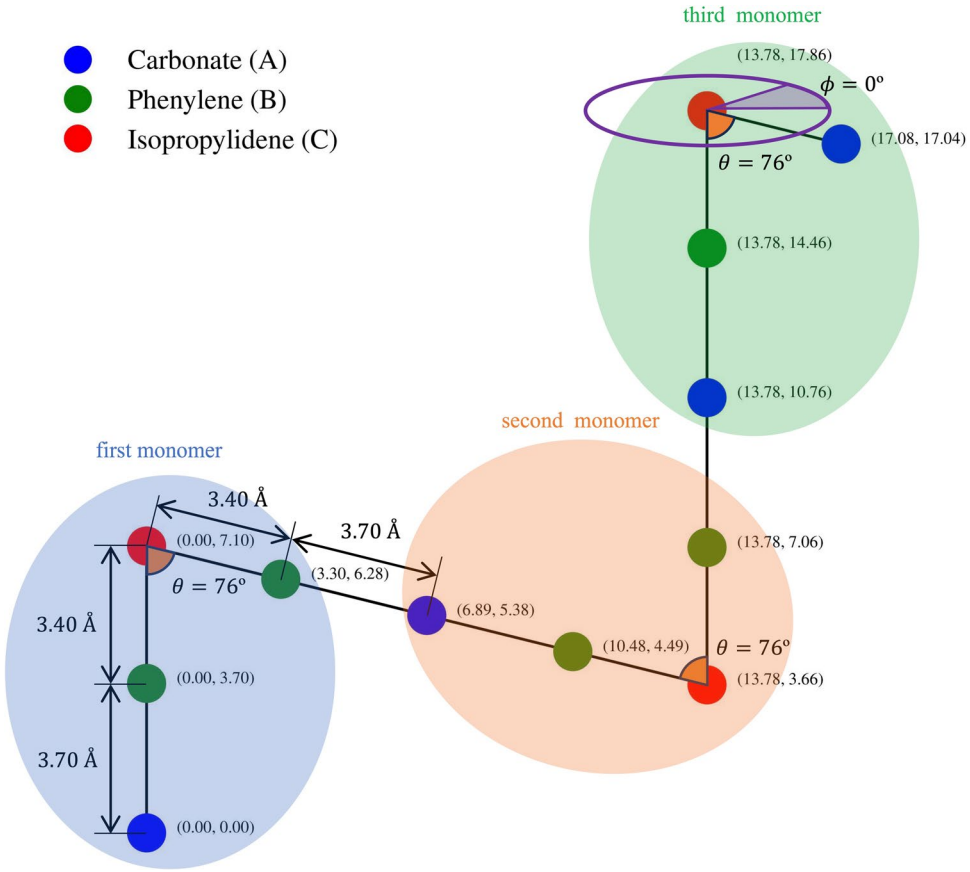

Fig. 2 Schematic of polycarbonate configuration. Carbonate, phenylene, and isopropylidene particles are labeled blue, green, and red circles, respectively. All bond lengths and bond angles (θ) are constrained with equilibrium bond lengths and bond angles; see Table 1. The angles of 180 degrees are not labeled in the figure. Each monomer is connected on the same two-dimensional plane, i.e. torsional angle (ϕ) = 0 degree (only shown in the third monomer)

where N_c and M_j are the numbers of molecular chains and mass of molecule j, respectively.

To examine the combinatory effect of spatial distribution and polydispersity on molecular behavior, each case of polydispersity was created with eight different radii of gyration by giving eight different segment lengths: 2, 4, 6, 8, 12, 16, 24, and 32 monomers. Noting that the segment length is directly proportional to the radius of gyration, see [13] for more details. Ten initial structures of each segment length case are reproduced with different random seeds to cope with stochastic deviation. In total, 720 models of polycarbonate structure are investigated in this study, calculated by the number of polydispersities × the number of segment lengths × the number of random seeds ($9 \times 8 \times 10 = 720$ structures).

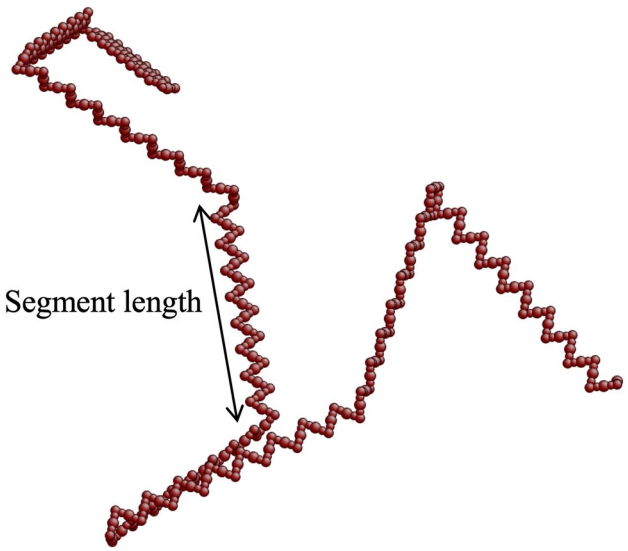

Fig. 3 Polycarbonate molecule with a segment length of 16 monomers (all types of particles are colored red)

The initial structures of the polycarbonate system were prepared according to the above mass distributions and segment lengths. The structures were equilibrated at 1000 K for 0.1 ns using the isothermal-isobaric ensemble (NPT), then cooled down to 300 K at a rate of 1000 K/ns. Finally, the structures were under NPT ensemble at 300 K for 1 ns for the equilibration. The time step of the calculation is 1 fs in all simulations. A three-dimensional periodic boundary condition was implemented. All simulations were performed using a Large-scale Atomic/Molecular Massively Parallel Simulator (LAMMPS) [30, 31] and were visualized using Open Visualization Tool (OVITO) [32].

Apart from R_g^n, molecular entanglement plays an important role in determining polycarbonate's deformation and fracture behavior [7, 12, 13]. The average number of

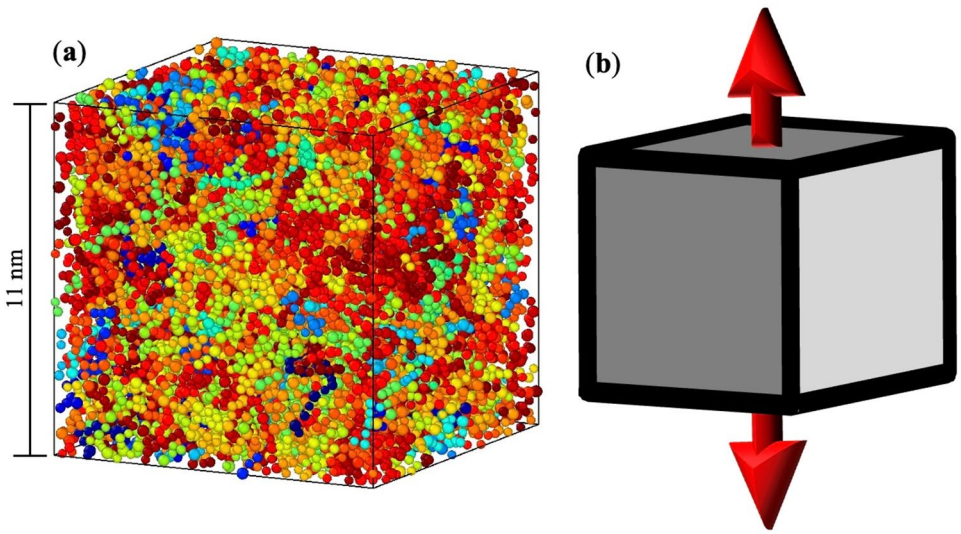

Fig. 4 **a** Simulation cell before deformation - each color represents an individual molecule. **b** Schematic of uniaxial tensile deformation

entanglement points (Z_e) per molecule was evaluated using the Z1 code [33–37]. The averaged molecular properties (R_g^n and Z_e) among ten structures of each polydispersity and segment length are shown in Table 3. The molecular parameters of each segment length across different polydispersities fall within the same range. R_g^n significantly increases as segment length, while Z_e shows only a slight decrease.

Representative molecular structures

For explanation, in the result ("Results" section), the true stress-strain curves and molecular structure development of only four representative structures are described. The combination of each of the lowest spatial distribution (segment length of 2 monomers) of monodisperse (PDI = 1.00) and polydisperse (PDI = 1.56) and the highest spatial distribution (segment length of 32 monomers) of monodisperse and polydisperse were investigated, which were denoted as ML, MH, PL, and PH, respectively. The molecular properties of the representatives are shown in Table 4.

Deformation analysis setup

Monotonic loading uniaxial tension simulations under the NPT ensemble were performed on all the simulation cells by induced external strain at a constant true strain rate, $d\varepsilon/dt = 2.398 \times 10^{-6}$ fs^{-1}, on the loading direction from true strain $\varepsilon = 0$ to 2.398 for 10^6 timesteps of 1 fs. In the other two lateral directions, the pressure is controlled at 1 atm during the deformation, see Fig. 4b. The simulations are carried out under an isothermal temperature of 300 K. The study adopted a true strain rate rather than an engineering strain rate because, from the experimentation, the strain-hardening of glassy polymer is closely related to a constant true strain rate [38].

Table 2 Details and molecular distribution of simulation cell

PDI	M_n	M_w	Number of molecule (-)			Total number of monomer
(-)	(kg/mol)	(kg/mol)	32-mer	128-mer	224-mer	(-)
1.00	32.8	32.8	0	32	0	4096
1.07	32.8	35.0	2	28	2	4096
1.14	32.8	37.3	4	24	4	4096
1.21	32.8	39.6	6	20	6	4096
1.28	32.8	41.9	8	16	8	4096
1.35	32.8	44.1	10	12	10	4096
1.42	32.8	46.4	12	8	12	4096
1.49	32.8	48.7	14	4	14	4096
1.56	32.8	51.0	16	0	16	4096

Table 3 Average molecular properties of molecular structures

$\mathbf{R}_g^n$ ($\mathbf{\AA/\sqrt[2]{kg/mol}}$)	Segment Length (-)							
PDI (-)	2	4	6	8	12	16	24	32
1.00	8.48	11.43	14.15	15.78	19.25	22.39	16.79	30.17
1.07	8.47	11.86	13.86	15.76	19.15	21.86	26.26	30.10
1.14	8.43	11.58	13.84	16.24	19.32	21.73	26.57	30.21
1.21	8.37	11.83	13.85	16.25	18.96	21.61	25.86	29.19
1.28	8.57	11.70	13.69	15.87	19.09	21.82	25.54	29.45
1.35	8.39	11.19	13.64	15.68	18.72	21.38	25.10	29.02
1.42	8.47	11.94	13.85	15.56	18.67	21.06	25.29	29.11
1.49	8.55	11.60	13.46	15.50	18.62	21.00	25.08	28.57
1.56	8.51	11.32	13.71	15.64	18.41	20.94	24.53	27.89
$\mathbf{Z}_e$ (**−/molecule**)	Segment Length (-)							
PDI (-)	2	4	6	8	12	16	24	32
1.00	47.77	49.35	47.61	45.53	42.62	39.47	37.73	35.20
1.07	49.45	49.61	48.14	45.68	42.53	40.04	37.23	35.20
1.14	48.71	49.52	47.92	46.21	42.86	39.80	36.90	34.59
1.21	50.50	50.58	48.48	46.73	42.74	40.25	38.49	35.49
1.28	48.24	50.62	49.08	47.05	43.52	41.18	37.28	35.10
1.35	50.78	51.76	49.11	46.77	43.23	40.62	38.48	35.57
1.42	50.86	50.72	49.52	47.65	43.78	40.02	38.29	35.41
1.49	51.74	51.36	50.24	46.83	43.50	40.67	37.83	34.61
1.56	51.26	51.37	51.02	48.16	43.58	40.17	38.35	35.02

Calculation and concept of nonaffine particle displacement

Nonaffine particle displacement ($\mathbf{r}_i^{na}$) is calculated as the deviation between the current position and the affine position from the reference of the particle i. The affine position is the product of the stretch ratio and the position of the particle at the reference frame, which is at zero strain in this study. For the structure at a certain stretch ratio (λ), nonaffine particle displacement compared to the initial structure can be described as:

$$\mathbf{r}_i^{na}(\lambda) = \mathbf{r}_i(\lambda) - \lambda \mathbf{r}_i(0), \tag{5}$$

where $\mathbf{r}_i^{na}$, $\mathbf{r}_i$, and $\mathbf{r}_i(0)$ are nonaffine particle displacement, the position, and the initial position of particle i, respectively.

Table 4 Properties of representative molecular structures

Case	PDI (-)	R_g^n ($\mathrm{\AA/\sqrt[2]{kg/mol}}$)	Z_e (-/molecule)	G_r (MPa)	α (-)
ML	1.00	8.56	44.56	36.89	0.000
MH	1.00	28.71	35.12	403.84	0.158
PL	1.56	8.68	51.66	33.65	0.000
PH	1.56	27.41	35.28	348.33	0.191

To understand the connection between the nonaffine particle displacement and local plastic activity, we assume that a typical structure undergoes a bulk stretch with a ratio of 2.0. The microscopic distance between two particles must be doubled in length if they are purely affine transformed. However, the intermolecular and intramolecular interactions counteract and restrain purely affine transformation. The more nonaffine particle displacement, the more stress is required to move that particle further and relates to effective chain stiffness [39]. Nonaffine particle displacement is detectable to a minimal extent within the elastic region, but becomes largely measurable in the plastic region, thereby describing local plastic deformation through nonaffinity. To describe the nonaffine particle displacement of the bulk structure, the root-mean-square of all particles in the structure is used and expressed as:

$$\mathbf{r}^{na}(\lambda) = \sqrt[2]{\mathbf{r}_i^{na}((\lambda))^2}. \tag{6}$$

Eindhoven Glassy Polymer model

The post-yield behavior of polycarbonate undergoes strain-hardening, described by the increase in stress after yielding at large strain, which is attributed to the entanglement

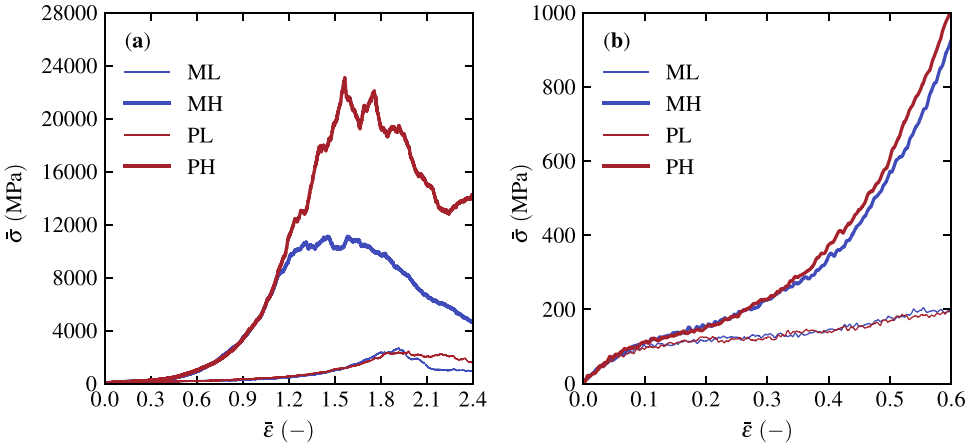

Fig. 5 True stress-strain ($\bar{\sigma}$-$\bar{\varepsilon}$) relationships of representative structures: **a** true strain ($\bar{\varepsilon}$) from 0.0 to 2.4 and **b** true strain ($\bar{\varepsilon}$) from 0.0 to 0.6

network of polymeric molecules during the deformation. The EGP model successfully captures the strain-hardening response of polycarbonate in the experiment by employing the Edwards-Vigils description in the molecular view [4, 40]. The simplified expression of true strain-hardening stress ($\bar{\sigma}_{\mathrm{H}}$) in isochoric uniaxial tension can be written as

$$\bar{\sigma}_{\mathrm{H}} = G_{\mathrm{r}}\left(\lambda^2 - \lambda^{-1}\right)\left[\frac{\alpha^2\left(1-\alpha^2\right)\left(\lambda^2+2\lambda^{-1}\right)}{\left(1-\alpha^2\left(\lambda^2+2\lambda^{-1}\right)\right)^2} + \frac{1-2\alpha^2}{1-\alpha^2\left(\lambda^2+2\lambda^{-1}\right)}\right], \tag{7}$$

where λ is the stretch ratio defined as the ratio between the current length and the initial length. G_{r} and α fitting constant parameters of EGP, representing strain-hardening modulus and chain extensibility. The expression is evaluated by assuming the mobility of entanglement is chosen to be zero. $\bar{\sigma}_{\mathrm{H}}$ is defined only in the post-yield region; $\bar{\sigma}_{\mathrm{H}} = \bar{\sigma} - \bar{\sigma}_{\mathrm{Y}}$, where $\bar{\sigma}$ is an observable true stress and $\bar{\sigma}_{\mathrm{Y}}$ is a yield stress. It is noteworthy that, in the case of α is chosen to be zero, the expression of strain-hardening stress (Eq. 6) reduces to a well-established neo-Hookean model [29], showing a linear relationship between strain-hardening stress $\bar{\sigma}_{\mathrm{H}}$ and the polynomial of stretch ratio $\left(\lambda^2 - \lambda^{-1}\right)$, i.e., $\bar{\sigma}_{\mathrm{H}} = G_{\mathrm{r}}\left(\lambda^2 - \lambda^{-1}\right)$. The strain-hardening modulus G_{r} is the slope of the relationship. Hence, the nonlinearity is solely attributed to the chain extensibility.

Results

Stress-strain relationship and strain-hardening & fracture behaviors

Figure 5 depicts the true stress-strain ($\bar{\sigma}$-$\bar{\varepsilon}$) relationships of four representative structures, namely ML, MH, PL, and PH. The magnification of a region with a relatively small strain from 0.0 to 0.6 is displayed in Fig. 5b, revealing that polydispersity and the normalized radius of gyration have a negligible effect on the elastic behavior and yield stress. Due to unclear yielding behavior, we adopt the scheme introduced in our previous work to evaluate yield stress [7]. Nonetheless, in the post-yielding region, it is evident that the stress increases with a higher strain-hardening rate in the structure with a higher normalized radius of gyration, whereas the stress slightly increases in the structure with a lower normalized radius of gyration. The variation in polydispersity does not affect the deformation behavior in the low-strain region. The significant difference in the strain-hardening rate between the structures with a high and low normalized radius of gyration highlights the influence of chain distribution on the post-yielding strain-hardening behavior. In particular, the higher strain-hardening rate in the highly dispersed structures suggests that the chains undergo a more significant degree of nonaffine stretching, leading to higher resistance to deformation. Figure 6 displays

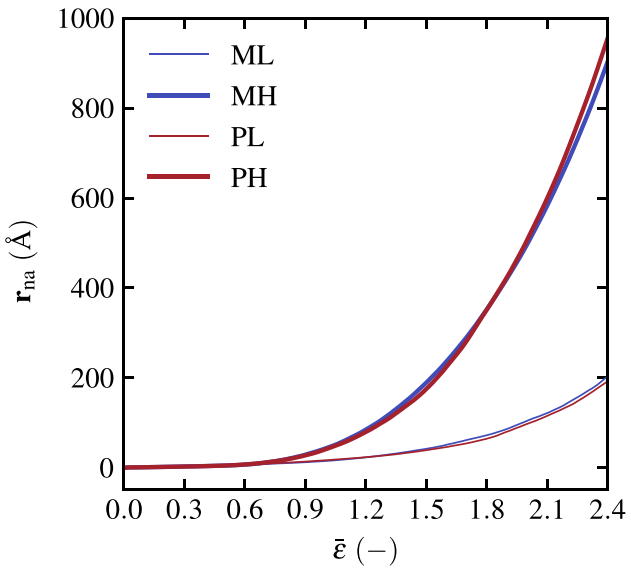

Fig. 6 Nonaffine particle displacement ($\mathbf{r}^{\mathrm{na}}$) as a function of true strain ($\bar{\varepsilon}$)

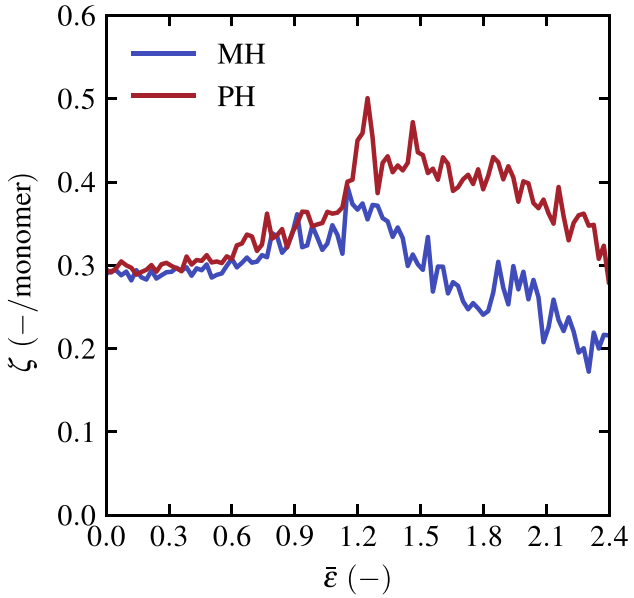

Fig. 7 Number of entanglements per monomer (ζ) as a function of true strain ($\bar{\varepsilon}$) from for the case of MH and PH

the nonaffine particle displacement of four representative structures during the deformation. Observation of nonaffine particle displacement during the deformation reveals that nonaffine particle displacement of the structures with a higher normalized radius of gyration increases at a higher rate than those with a lower normalized radius of gyration. Since more stress is required to translate nonaffine particles [10], stresses of the cases MH and PH increase significantly. After the strain-hardening region, all the structures attain maximum stress, namely fracture.

The $\bar{\sigma}$-$\bar{\varepsilon}$ relationships of the cases ML and PL are similar, and so are the maximum stress values at around 2500 MPa. On the other hand, among the higher normalized radius of gyration structures (MH and PH), the stress-strain relationships are parallel from the beginning to around true strain = 1.10. Then, the case of MH separates and fractures soon at 11,000 MPa, but the case of PH continues strain-hardening and approaches maximum stress at 23,000 MPa. The polydispersity has a significant effect on the maximum stress of the high normalized radius of gyration polycarbonate system. The increment is attributed to the number of entanglements in the polymeric system. It is noted here that the observable maximum stress is remarkably high, especially in the case of PH. The value of 23,000 MPa is comparable with the theoretical strength of the ideal chemical bonds [7]. Therefore, the bond-breaking may be effective in the actual situation, but for simplicity, we did not simulate the effect.

Figure 7 reveals the development of the number of entanglements per monomer during the deformation, $\zeta = Z/N_m$, where Z and N_m are the total numbers of entanglements and monomers in the structure, respectively. In the cases of MH and PH, both display a consistent pattern of ζ, from a similar starting value at around 0.3 entanglements per monomer and gradually increase between the range of true strain from 0.0 to 1.1, indicating a strong correlation between increments of stress and entanglements. From the observation around $\bar{\varepsilon} = 1.2$, an abrupt increase of ζ is observed, which suggests the formation of the entanglements. The more entanglements are formed, the more degree of strain-hardening arises. In the case of PH, ζ increases upon 0.5 entanglements per monomer, but in the case of MH reaches a maximum of 0.4 entanglements per monomer. Even with the same initial amount of entanglement, the development of ζ under deformation is affected by polydispersity, particularly in the cases with a large normalized radius of gyration.

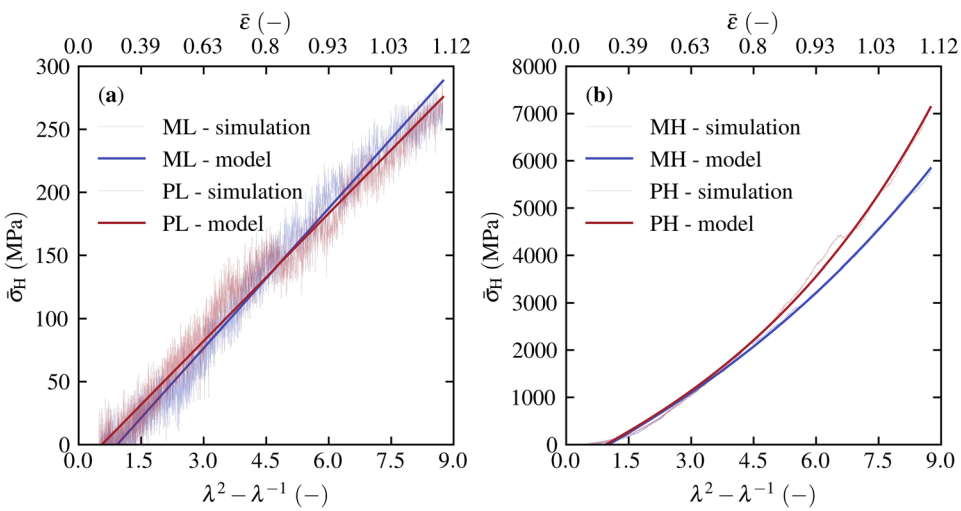

Fig. 8 Strain-hardening stress ($\bar{\varepsilon}_H$) from the simulation and from the model as a function of the polynomial of stretch ratio $\left(\lambda^2 - \lambda^{-1}\right)$ from 0.0 to 9.0 and $\bar{\varepsilon}$ from 0.0 to 1.12 (labeled nonlinearly) for **a** the cases of ML and PL and **b** the cases of MH and PH

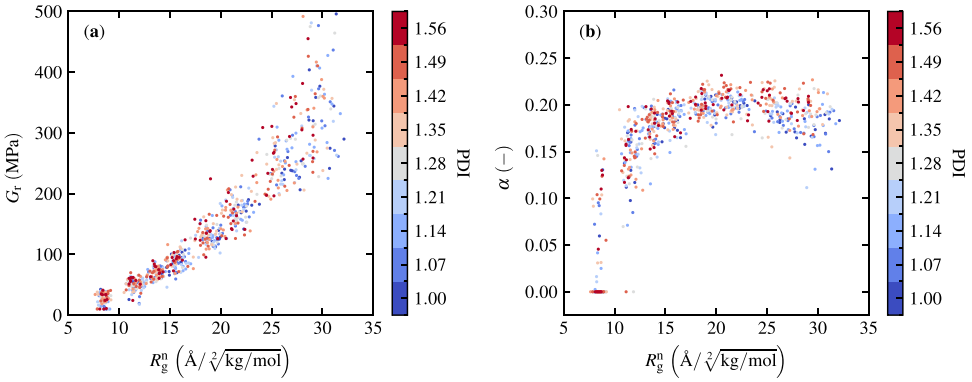

Fig. 9 Fitting parameters of as a function of the normalized radius of gyration (R_g^n): **a** Strain-hardening modulus (G_r) and **b** Chain extensibility (α). Colors represent different polydispersities (PDI)

Effect of molecular structure on strain-hardening modulus and chain extensibility

From the observation of the true stress-strain relationship, the strain-hardening stress is obtained by subtracting yield stress from true stress. Figure 8 reveals the relationship between strain-hardening stress $\bar{\sigma}_H$ and the polynomial of stretch ratio $\left(\lambda^2 - \lambda^{-1}\right)$ from the simulation data and the EGP model fitting, ranging from post-yielding to pre-fracture region. The fitting parameters (G_r and α) are reported in Table 4. Figure 8a shows the cases of ML and PL, in which the relationship is essentially linear because, from the fitting, chain extensibilities are approximately zero, see Table 4. Figure 8b reveals the nonlinear response of $\bar{\sigma}_H$ as a function $\left(\lambda^2 - \lambda^{-1}\right)$ in two cases, MH and PH. The results suggest that the structure with a higher initial radius of gyration exhibits a higher strain-hardening modulus and chain extensibility.

The EGP model fitting is applied to all 720 structures in this research. Figure 9 shows the relationship between fitting parameters and the initial normalized radius of gyration. Figure 9a indicates that G_r has a parabolic relationship with the R_g^n and is independent of polydispersity. While only a small variation of G_r is observed in lower R_g^n, G_r variates more widely in higher R_g^n. Due to the sensitivity of G_r to the initial number of entanglements, the observed wide variation is attributed to the differences in the number of entanglements within the polymeric system, which were not investigated in this study. Taking into account the direct proportionality between the strain-hardening modulus and the true strain rate [41], the values of G_r resulting from the simulation notably exceed those determined through experimentation. Figure 9b shows that the chain extensibility cannot be observed in the structure with lower R_g^n (less than $10/\sqrt[2]{\text{kg/mol}}$). The chain extensibility increases as R_g^n increases and is saturated at around 0.20. No structure has α higher than 0.25. The values obtained from the model fitting are comparable with the values from the experimentation fitting, i.e., 0.23 [4].

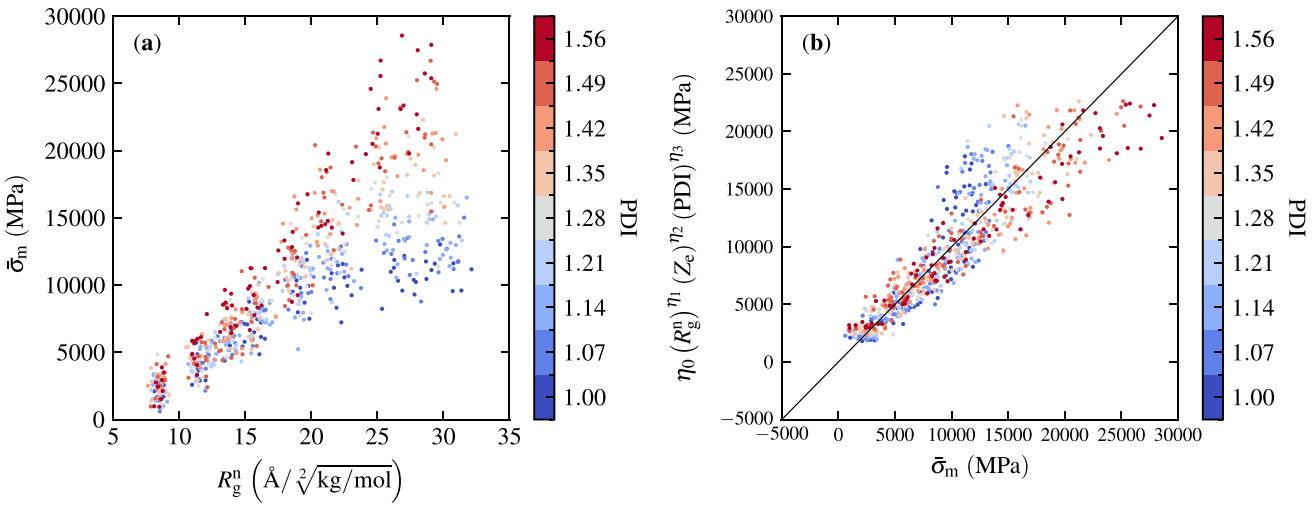

Fig. 10 **a** Maximum stress ($\bar{\sigma}_m$) as a function of and R_g^n and colors show different PDIs. **b** Correlation between $\bar{\sigma}_m$ and its power law phenomenological expression, with four fitting parameters: $\eta_0 = 0.203$ MPa, $\eta_1 = 1.738$, $\eta_3 = 0.642$, and $\eta_4 = 0.765$. The color bars represent different PDIs

Effect of molecular structure and polydispersity on maximum stress

Figure 10a depicts maximum stress ($\bar{\sigma}_m$) as a function of the normalized radius of gyration for different polydispersities of all 720 structures. The maximum stresses at R_g^n of less than $(10/\sqrt[2]{\mathrm{kg/mol}})$ of different PDIs exhibit the same range below 5000 MPa. As R_g^n increases, the maximum stress of the higher PDI structure increases at a higher rate than that of the relatively lower PDI structure. The monodisperse structure exhibits maximum stresses that are confined to approximately 10000 MPa, while the polydisperse structure displays a significant increase in maximum stresses, reaching up to 25000 MPa.

According to our previous investigation, the phenomenological relationship between maximum stress, the normalized radius of gyration, and the average entanglements per molecule (Z_e) follows the power law relationship [13]. In addition to the previous model, the PDI is added to the relationship can be written as

$$\bar{\sigma}_m = \eta_0 \left(R_g^n\right)^{\eta_1} \left(Z_e\right)^{\eta_2} (\mathrm{PDI})^{\eta_3}, \tag{8}$$

with four fitting parameters: $\eta_0 = 5.264$ MPa, $\eta_1 = 1.774$, $\eta_2 = 0.536$, and $\eta_3 = 0.947$. Figure 10b shows the relationship between the values from simulation and power law model. This phenomenological expression suggests that not only R_g^n and Z_e have a significant effect on maximum stress, but PDI also describes the fracture of polycarbonate. The expression only encourages the direction for further investigation of the connection between a macroscopic maximum stress and molecular parameters in the future.

Conclusion

In this study, we aim to investigate the effect of initial spatial distribution and polydispersity on the strain-hardening and fracture behavior of polycarbonate. We obtain a better understanding of deformation behavior by performing a series of CGMD uniaxial tensile deformations of polycarbonate with various initial radii of gyration and polydispersities. The structure with a larger radius of gyration exhibits a higher strain-hardening modulus and chain extensibility, while PDI has no effect on strain-hardening response. However, PDI has a positive correlation with maximum stress, which is attributed to the ability to maintain the entanglements of long chains in more significant strains. Lastly, the phenomenological relationship between molecular parameters and maximum stress is suggested to convey and inspire future investigation in this field.

Appendix A. Validation of simulation cell size

The validation of the selected simulation cell size (approximately 11 nm in length) employed in the present study is addressed through a comparative analysis involving structures of varying dimensions: 113 Å and 906 Å. The methodology applied for these structures is consistent with the approach described in "Coarse-grained particle arrangement and radius of gyration control" section, and they both undergo the same deformation setup as described in "Deformation analysis setup" section. Notably, the length of the simulation cell of the latter structure surpasses the radius of gyration by more than five times as recommended in the former literature [42]. The true stress-true strain relationship of these two structures subjected to the deformation is depicted in Fig. 11. Remarkably, significant differences in both the maximum true stress and the strain-hardening behavior between the two structures are absent. Although the larger simulation cell size results in less stress fluctuation during deformation, it culminates in a comparable maximum true stress value at around 12000 MPa.

This phenomenon can be attributed to the influence of the microscale void present in the structure characterized by the larger radius of gyration. The cell size plays an important role in constraining the void's dimensions during the deformation simulation; excessively diminutive cell sizes may yield erroneous outcomes. Conversely, when dealing with structures possessing large radii of gyration, the voids manifest a finely distributed nature in a small size [13]. Consequently, the impact of the simulation cell size on the overall behavior becomes marginal in investigating maximum stress and strain-hardening behavior.

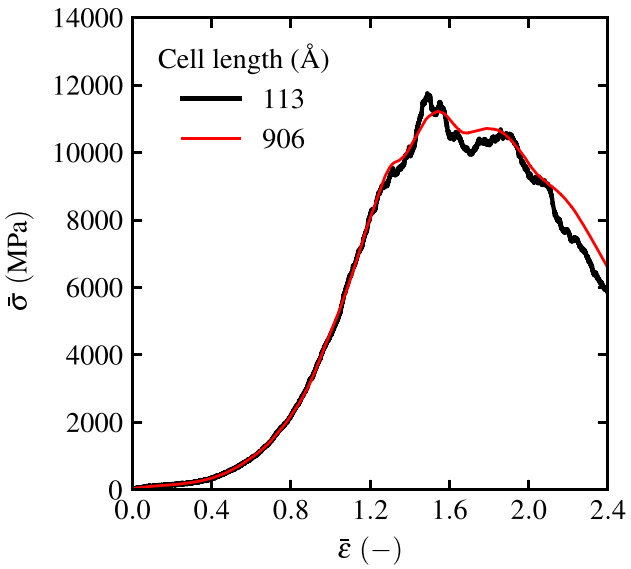

Fig. 11 True stress-true strain curves of structure with two simulation cell sizes of 113 Å (black) and 906 Å (red)

Appendix B. Validation of cooling rate

During the equilibration process, where artificial deterministic particle positions transition into a more realistic stochastic distribution, there are three distinct sub-processes. Firstly, an isobaric-isothermal (NPT) ensemble is maintained for 0.1 ns at 1000 K. Subsequently, the system experiences cooling within the NPT ensemble, transitioning from 1000 K to 300 K over a duration of 0.7 ns, resulting in a cooling rate of 1000 K/ns. Lastly, the system is further equilibrated in an NPT ensemble at 300 K for an additional 1 ns.

The validation of the selected cooling rate (1000 K/ns) employed in the present study is addressed through a comparative analysis involving structures of two cooling rates during equilibrium process. The structures are cooled down from 1000 K to 300 K with 1.4 ns and 0.7 ns or cooling rates of 500 K/ns and 1000 K/ns, respectively. The former cooling rate is performed to consider whether, or not, the cooling rate affects nonaffine displacement parameter during the deformation. The latter cooling rate is values applied throughout the study. The two cooling rates are subjected to the structures of low (L) and high (H) radii of gyration. Figure 12 shows the development of nonaffine particle displacement during the deformation of four structures. The result implies that there is no difference in nonaffine particle displacement due to changes in cooling rate.

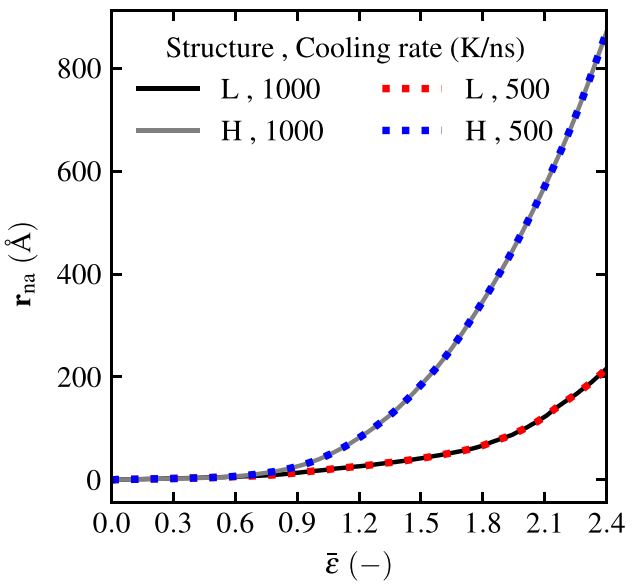

Fig. 12 Nonaffine particle displacement ($\mathbf{r}^{na}$) as a function of true strain ($\bar{\varepsilon}$) of structure with different radii of gyration and cooling rate. The structures of low (L) and high (H) radii of gyration have values of 47 Å and 170 Å, respectively. The cooling rates are 500 K/ns (dotted) and 1000 K/ns (line)

Acknowledgements This work was supported by Core Research and Evolutionary Science and Technology (CREST) under the Japan Science and Technology Agency (JST) [Grant No. JPMJCR2092]. The author, T. Leelaprachakul, gratefully acknowledges the financial support from the World-leading Innovative Graduate Study Program on Global Leadership for Social Design and Management (WINGS-GSDM) [Grant No. 21204]. The author, A. Kubo, acknowledges the financial support from the Foundation for Promotion of Material Science and Technology of Japan (MST) [Grant No. 383].

Author contributions Tatchaphon Leelaprachakul: Conceptualization, Methodology, Software, Validation. Formal analysis, Investigation, Data Curation, Writing – Original Draft, Visualization. Atsushi Kubo: Software, Formal analysis, Writing – Review & Editing. Yoshitaka Umeno: Resources, Writing – Review & Editing, Project administration, Funding acquisition.

Funding Open access funding provided by The University of Tokyo.

Data availability The data that support the findings in this study are available from the corresponding author upon reasonable request.

Declarations

Competing interests The authors declare that they have no known competing financial interests or personal relationships that could have appeared to influence the work reported in this paper.

References

1. Zhang W, Xu Y (2019) Introduction. In: Mechanical Properties of Polycarbonate, pp 11–27. Elsevier, Radarweg 29, 1043 NX Amsterdam, The Netherlands. https://doi.org/10.1016/B978-1-78548-313-4.50009-1
2. Wang X, Zheng X, Song M, Wu S (2014) A study on the relationship between polycarbonate microstructure and performance as determined by a combined experimental and molecular dynamics simulation method. e-Polymers 14:407–415. https://doi.org/10.1515/epoly-2014-0065
3. Kattekola B, Desai CK, Parameswaran V, Basu S (2014) Experimental Mechanics 54(3):357–368. https://doi.org/10.1007/s11340-013-9810-x
4. Senden DJA, Krop S, Dommelen JAW, Govaert LE (2012) Rate- and temperature-dependent strain hardening of polycarbonate. J Polym Sci B: Polym Phys 50:1680–1693. https://doi.org/10.1002/polb.23165

5. Duan Y, Saigal A, Greif R, Zimmerman MA (2001) A uniform phenomenological constitutive model for glassy and semicrystalline polymers. Polym Eng Sci 41(8):1322–1328. https://doi.org/10.1002/pen.10832
6. Xu Y, Gao T, Wang J, Zhang W (2016) Experimentation and modeling of the tension behavior of polycarbonate at high strain rates. Polymers 8(3). https://doi.org/10.3390/polym8030063
7. Umeno Y, Kubo A, Albina J-M (2020) Coarse-grained molecular dynamics simulation of deformation and fracture in polycarbonate: Effect of molar mass and entanglement. Theor Appl Fract Mech 109:102699. https://doi.org/10.1016/j.tafmec.2020.102699
8. Govaert LE, Tervoort TA (2004) Strain hardening of polycarbonate in the glassy state: Influence of temperature and molecular weight. J Polym Sci B: Polym Phys 42:2041–2049. https://doi.org/10.1002/polb.20095
9. Tervoort TA, Govaert LE (2000) Strain-hardening behavior of polycarbonate in the glassy state. J Rheol 44:1263–1277. https://doi.org/10.1122/1.1319175
10. Vorselaars B, Lyulin AV, Michels MAJ (2009) Microscopic mechanisms of strain hardening in glassy polymers. Macromolecules 42:5829–5842. https://doi.org/10.1021/ma802709d
11. Hoy RS, Robbins MO (2008) Strain hardening of polymer glasses: Entanglements, energetics, and plasticity. Phys Rev E 77:031801. https://doi.org/10.1103/PhysRevE.77.031801
12. Leelaprachakul T, Kubo A, Umeno Y (2022) Coarse-grained molecular dynamics simulation of fracture in polycarbonate: Fracture stress prediction from molecular entanglement and spatial distribution. Zairyo/J Soc Mater Sci, Japan 71. https://doi.org/10.2472/jsms.71.151
13. Leelaprachakul T, Kubo A, Umeno Y (2023) Coarse-grained molecular dynamics simulation of polycarbonate deformation: Dependence of mechanical performance by the effect of spatial distribution and topological constraints. Polymers 15. https://doi.org/10.3390/polym15010043
14. Baschnagel J, Binder K, Paul W, Laso M, Suter UW, Batoulis I, Jilge W, Bürger T (1991) On the construction of coarse-grained models for linear flexible polymer chains: Distribution functions for groups of consecutive monomers. J Chem Phys 95:6014–6025. https://doi.org/10.1063/1.461826
15. Tang Z, Fujimoto K, Okazaki S (2020) All-atom molecular dynamics study of impact fracture of glassy polymers. ii: Microscopic origins of stresses in elasticity, yielding, and strain hardening. Polymer 207. https://doi.org/10.1016/j.polymer.2020.122908
16. Fujimoto K, Tang Z, Shinoda W, Okazaki S (2019) All-atom molecular dynamics study of impact fracture of glassy polymers. i: Molecular mechanism of brittleness of pmma and ductility of pc. Polymer 178. https://doi.org/10.1016/j.polymer.2019.121570
17. Sahputra IH, Echtermeyer A (2021) The effects of the van der Waals potential energy on the young's modulus of a polymer: Comparison between molecular dynamics simulation and experiment. J Polym Res 28:47. https://doi.org/10.1007/s10965-021-02413-4
18. Fujimoto K (2022) Fracture and toughening mechanisms of glassy polymer at the molecular level. Nihon Reoroji Gakkaishi 50:37–41. https://doi.org/10.1678/rheology.50.37
19. Kubo A, Albina JM, Umeno Y (2019) Construction of master yield stress curves for polycarbonate: a coarse-grained molecular dynamics study. Polymer 177:84–90. https://doi.org/10.1016/j.polymer.2019.05.045
20. Palczynski K, Wilke A, Paeschke M, Dzubiella J (2017) Molecular modeling of polycarbonate materials: Glass transition and mechanical properties. Phys Rev Mater 1. https://doi.org/10.1103/PhysRevMaterials.1.043804
21. Hess B, León S, Vegt NVD, Kremer K (2006) Long time atomistic polymer trajectories from coarse grained simulations: Bisphenol-a polycarbonate. Soft Matter 2:409–414. https://doi.org/10.1039/b602076c
22. Zhu P, Lin J, Xiao R, Zhou H (2022) Unravelling physical origin of the bauschinger effect in glassy polymers. J Mech Phys Solids 168. https://doi.org/10.1016/j.jmps.2022.105046
23. León S, Vegt N, Site LD, Kremer K (2005) Bisphenol a polycarbonate: Entanglement analysis from coarse-grained md simulations. Macromolecules 38:8078–8092. https://doi.org/10.1021/ma050943m
24. Ikeshima D, Miyamoto K, Yonezu A (2019) Molecular deformation mechanism of polycarbonate during nano-indentation: Molecular dynamics simulation and experimentation. Polymer 173:80–87. https://doi.org/10.1016/j.polymer.2019.04.029
25. Ikeshima D, Yonezu A, Liu L (2018) Molecular origins of elastoplastic behavior of polycarbonate under tension: a coarse-grained molecular dynamics approach. Comput Mater Sci 145:306–319. https://doi.org/10.1016/j.commatsci.2018.01.001
26. Nunes RW, Martin JR, Johnson JF (1982) Influence of molecular weight and molecular weight distribution on mechanical properties of polymers. Polym Eng Sci 22:205–228. https://doi.org/10.1002/pen.760220402
27. Dobkowski Z (1982) Influence of molecular weight distribution and long chain branching on the glass transition temperature of polycarbonate. Eur Polym J 18:563–567. https://doi.org/10.1016/0014-3057(82)90032-5
28. Dobkowski Z (1995) Determination of critical molecular weight for entangled macromolecules using the tensile strength data. Rheologica Acta 34:578–585. https://doi.org/10.1007/BF00712317
29. Haward RN (1993) Strain hardening of thermoplastics. Macromolecules 26:5860–5869. https://doi.org/10.1021/ma00074a006
30. Plimpton S (1995) Fast parallel algorithms for short-range molecular dynamics. J Comput Phys 117:1–19. https://doi.org/10.1006/jcph.1995.1039
31. Thompson AP, Aktulga HM, Berger R, Bolintineanu DS, Brown WM, Crozier PS, Veld PJ, Kohlmeyer A, Moore SG, Nguyen TD, Shan R, Stevens MJ, Tranchida J, Trott C, Plimpton SJ (2022) Lammps - a flexible simulation tool for particle-based materials modeling at the atomic, meso, and continuum scales. Comput Phys Commun 271. https://doi.org/10.1016/j.cpc.2021.108171
32. Stukowski A (2010) Visualization and analysis of atomistic simulation data with ovito-the open visualization tool. Model Simul Mater Sci Eng 18. https://doi.org/10.1088/0965-0393/18/1/015012
33. Kröger M (2005) Shortest multiple disconnected path for the analysis of entanglements in two- and three-dimensional polymeric systems. Comput Phys Commun 168:209–232. https://doi.org/10.1016/j.cpc.2005.01.020
34. Shanbhag S, Kröger M (2007) Primitive path networks generated by annealing and geometrical methods: Insights into differences. Macromolecules 40:2897–2903. https://doi.org/10.1021/ma062457k
35. Hoy RS, Foteinopoulou K, Kröger M (2009) Topological analysis of polymeric melts: Chain-length effects and fast-converging estimators for entanglement length. Phys Rev E 80:031803. https://doi.org/10.1103/PhysRevE.80.031803
36. Karayiannis NC, Kröger M (2009) Combined molecular algorithms for the generation, equilibration and topological analysis of entangled polymers: Methodology and performance. Int J Mol Sci 10:5054–5089. https://doi.org/10.3390/ijms10115054
37. Kröger M, Dietz JD, Hoy RS, Luap C (2023) The z1+ package: Shortest multiple disconnected path for the analysis of entanglements in macromolecular systems. Comput Phys Commun 283:108567. https://doi.org/10.1016/j.cpc.2022.108567
38. Bartczak Z (2005) Effect of chain entanglements on plastic deformation behavior of linear polyethylene. Macromolecules 38:7702–7713. https://doi.org/10.1021/ma050815y
39. MacNeill D, Rottler J (2010) From macroscopic yield criteria to atomic stresses in polymer glasses. Phys Rev E 81:011804. https://doi.org/10.1103/PhysRevE.81.011804

40. Edwards SF, Vilgis T (1986) The effect of entanglements in rubber elasticity. Polymer 27:483–492. https://doi.org/10.1016/0032-3861(86)90231-4
41. Chou SC, Robertson KD, Rainey JH (1973) The effect of strain rate and heat developed during deformation on the stress-strain curve of plastics. Exp Mech 13:422–432
42. Gartner TEI, Jayaraman A (2019) Modeling and simulations of polymers: a roadmap. Macromolecules 52(3):755–786. https://doi.org/10.1021/acs.macromol.8b01836